PNAS RESEARCH ARTICLE | PHYSICS

Elastic tricriticality at the collapse of magnetic order in a valence fluctuating Eu-based compound

Yassine Agarmani[a,1], Arif Ata[a], Lars Franke[b], Jan Zimmermann[a], Ulrich Tutsch[a], Marius Peters[a], Michelle Ocker[a], Kristin Kliemt[a], Cornelius Krellner[a], Bernd Wolf[a], Markus Garst[b], and Michael Lang[a]

Edited by J. C. Séamus Davis, University of Oxford, Oxford, United Kingdom; received April 24, 2026; accepted October 9, 2026

Spin and charge fluctuations are key for understanding the properties of materials with strongly correlated electrons, but their coupling to the atomic crystal lattice is often assumed to be weak and perturbative. In this work, we demonstrate that at tricritical points (TCPs), that are associated with electronic correlations, a coupling to crystal elasticity is generically nonperturbative. It will modify the tricritical universality class leading to *elastic tricriticality*, characterized by a compressibility that diverges in a universal manner with the correlation length. To test this scenario experimentally, we use single crystals of $EuPd_2(Si_{1-x}Ge_x)_2$ where, depending on x and pressure, magnetic order collapses due to strong valence fluctuations. First, we confirm the presence of a TCP for $x \approx 0.1$ by using complementary probes, in particular, measurements of relative length changes under control of temperature and He-gas pressure. Second, by studying the elastic response, we uncover clear signatures of elastic tricriticality, notably a drastically enhanced compressibility.

strongly correlated systems | critical phenomena | elasticity | rare-earth intermetallics

Materials with strongly correlated electrons are of continuing high interest due to the wealth of intriguing phenomena and the challenges they pose for the understanding of various instabilities and the role played by different types of fluctuations. Electron-electron correlations and the associated phase transitions can often be controlled by pressure. Key examples include the Mott metal-insulator transition (1) revealed, e.g., in transition-metal oxides (2, 3) and organic charge-transfer salts (4), as well as the valence transition in certain rare earth- and actinide materials including the γ - α transition in cerium (5–7), see, e.g., refs. 8 and 9 for early reviews. While these phenomena appear to be driven by strong electron-electron interactions, the high sensitivity to pressure indicates a pronounced coupling between electronic and lattice degrees of freedom.

Materials with Mott- or valence transitions have in common that their phase diagram contains a line of first-order phase transitions that terminates in a critical endpoint (CEP), see Fig. 1*A*. Close to the endpoint, the critical behavior is characterized by an emergent Ising order parameter ψ similar to the liquid-gas endpoint (10, 11). However, in a solid this order parameter will involuntarily couple to the atomic crystal lattice, and this elastic coupling changes the universality class of the CEP resulting in *critical elasticity* (12). Instead of a liquid-gas CEP, the long-range shear forces of the crystal give rise to an elastic solid-solid CEP that is governed by mean-field behavior without microscopic critical fluctuations and, therefore, it lacks a diverging correlation length. For the valence transition, this has been pointed out and experimentally confirmed early on for the γ - α transition in $Ce_{1-x}Th_x$ (6), see also refs. 13 and 14. For the Mott transition, experimental evidence was found in $(V_{1-x}Cr_x)_2O_3$ (3) as well as in the organic conductor κ-(BEDT-TTF)$_2$Cu[N(CN)$_2$]Cl (15), see also the discussion in refs. 16–19.

A more intricate situation arises when the electronic valence fluctuations (VF) are accompanied by critical spin fluctuations due to the vicinity of long-range magnetic order (20, 21). The interplay of these different types of fluctuations is considered key to understanding a variety of intriguing phenomena in correlated electron systems, including different types of unconventional superconductivity (see, e.g., ref. 22). In particular, it has been predicted that weak AFM order can be destabilized by strong valence fluctuations (21), resulting in a tricritical point (TCP) as schematically shown in Fig. 1*B*. This scenario is also corroborated by Landau theory, see *SI Appendix*, section H for details. At such a TCP, the second-order phase transition turns into a first-order transition accompanied by a crossover line.

Significance

When studying the rich diversity of phases characterizing materials with strongly correlated electrons, the underlying lattice is usually regarded as a weak perturbation to the interacting electrons. In this study, we show that this common view is violated at a tricritical point (TCP). At the TCP, the electron-lattice coupling becomes nonperturbatively strong, leading to elastic tricriticality. We observed its defining feature, a giant softening of the crystal lattice, in an europium-based material, precisely tuned to its TCP by pressure. Since the arguments for the emergence of elastic tricriticality are very general, our findings imply that similar strong-coupling effects should occur at any pressure-induced TCP at finite temperatures, forcing a new perspective on critical phenomena in many different classes of materials.

Author affiliations: [a]Institute of Physics, Goethe University Frankfurt, Frankfurt (M) 60438, Germany; and [b]Institute of Theoretical Solid State Physics, Karlsruhe Institute of Technology, Karlsruhe 76131, Germany

Author contributions: B.W. and M.L. designed research; Y.A., A.A., J.Z., U.T., M.P., M.O., K.K., C.K., B.W., and M.L. performed research; Y.A., A.A., L.F., J.Z., U.T., B.W., M.G., and M.L. analyzed data; L.F. and M.G. performed theoretical research; M.P., M.O., K.K., and C.K. contributed to sample growth and preparation; and Y.A., B.W., M.G., and M.L. wrote the paper.

The authors declare no competing interest.

This article is a PNAS Direct Submission.

Copyright © 2026 the Author(s). Published by PNAS. This article is distributed under Creative Commons Attribution-NonCommercial-NoDerivatives License 4.0 (CC BY-NC-ND).

[1]To whom correspondence may be addressed. Email: agarmani@physik.uni-frankfurt.de.

This article contains supporting information online at https://www.pnas.org/lookup/suppl/doi:10.1073/pnas.2614506123/-/DCSupplemental.

Published November 10, 2026.

Downloaded from https://www.pnas.org by KARLSRUHER INSTITUT FUER TECHNOLOGIE KIT on November 18, 2026 from IP address 129.13.194.163.

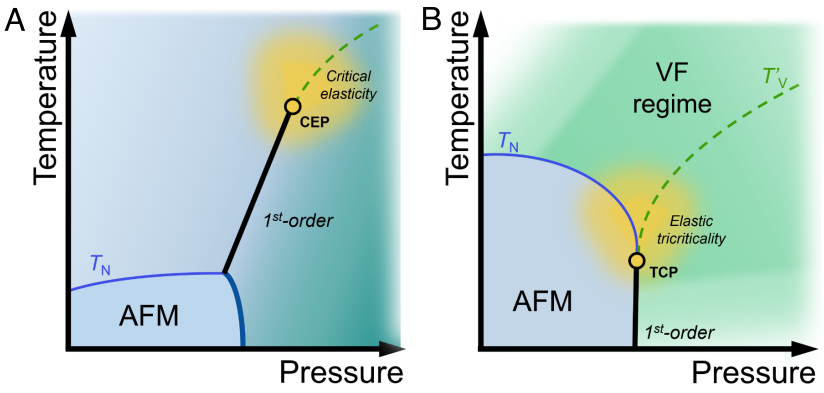


Fig. 1. Schematic temperature-pressure phase diagrams for materials with strongly correlated electrons featuring critical points. (*A*) A line of first-order transitions terminates in a critical endpoint (CEP) out of which a crossover line (broken line) evolves. Around the CEP *critical elasticity* (yellow-filled area) is expected. At low temperatures and low pressures, one often finds long-range antiferromagnetic (AFM) order. (*B*) A tricritical point (TCP) is revealed when a line of first-order transitions turns into a line of second-order transitions. This is accompanied by the appearance of a crossover line. As argued below, around the TCP one expects effects of *elastic tricriticality* (yellow area). A scenario, implying a TCP, has been proposed in which AFM order collapses due to the effect of strong valence fluctuations (VF): The second-order transition associated with AFM order below T_N (blue line) turns into a first-order transition (black solid line) upon merging with the valence-crossover line T'_V (green dashed line).

In the present work, we aim to elucidate the interplay between valence, spin, and elastic fluctuations, with particular emphasis on how the elastic coupling affects tricritical behavior materializing close to the TCP in Fig. 1*B*. We argue theoretically and we provide experimental evidence that the elastic coupling also changes the universality class of the TCP resulting in *elastic tricriticality*. In contrast to the elastic solid-solid CEP, however, critical microscopic fluctuations of the coupled electronic-elastic system are maintained at the elastic TCP, implying a diverging correlation length and universal critical exponents.

For the realization of a phase diagram with a TCP, Eu-based intermetallics may provide a suitable basis given their tendency to form charge-fluctuating, intermediate-valence states in close proximity to magnetic order (23–26). A particularly interesting case has been revealed by $EuPd_2(Si_{1-x}Ge_x)_2$. Instead of a first-order transition, generally observed at the valence instability (23, 26–30), $EuPd_2Si_2$ shows a continuous valence change (31–34) indicative of a crossover (35, 36). With increasing Ge substitution x, which acts as negative (chemical) pressure, the crossover temperature T'_V becomes reduced for small substitution levels ($x < 0.1$) before the material develops antiferromagnetic order at $x > 0.1$ (35, 36). Interestingly, studies on a single crystal with $x \approx 0.1$ performed at various pressures suggest that by applying a tiny amount of pressure on the order of 10 MPa, i.e., 0.1 per mille of the value of typical bulk moduli of metals, the antiferromagnetic order collapses via a first-order phase transition giving way to a state with strong valence fluctuations (35). These findings hint at the existence of a TCP, which, if confirmed, would open up the exciting possibility of exploring the impact of critical charge and spin fluctuations on the elastic properties and thus verifying elastic tricriticality.

The objectives of the present work are twofold. First, we confirm the presence of a TCP for $x \approx 0.1$ by using complementary probes. Second, we uncover clear signatures of elastic tricriticality by studying the elastic response of the material finely tuned to its TCP. We performed measurements of expansivity, resistivity, and magnetometry both as a function of temperature, T, at constant pressure, p, and vice versa, as a function of p at constant T. Our experiments were made possible, in particular, by recent technical developments that enable high-resolution measurements of relative length changes to be performed under continuous variation of He-gas pressure (37, 38).

Results

All samples used in this work were cut off from a single, large $EuPd_2(Si_{0.89}Ge_{0.11})_2$ crystal to minimize effects related to sample-to-sample variations (*SI Appendix*, Table S1 and Fig. S2).

In the following, we present results of expansivity, resistivity, and magnetometry. Given that the target material, $EuPd_2(Si_{1-x}Ge_x)_2$, crystallizes in the tetragonal $ThCr_2Si_2$ (122) structure (31) (*SI Appendix*, Fig. S1), and shows strongly anisotropic lattice effects at the valence change for $x = 0$, which are essentially governed by changes in the in-plane a axis (36, 39) (*SI Appendix*, Fig. S4*A*), our study focuses on probing the a axis expansivity.

Identification of the Tricritical Point. In Fig. 2*A*, we show exemplarily three datasets on $EuPd_2(Si_{0.89}Ge_{0.11})_2$ including the relative length change, $\Delta L_a(T, p = \text{const.})/L_a$ (*Top* panel), the change in resistivity, $\Delta\rho(T, p = \text{const.})/\rho$ (*Middle* panel), and the change in magnetic moment, $\Delta m_a(T, p = \text{const.})/m_a$ (*Bottom* panel), as a function of temperature, taken at two slightly different pressure values, resulting in distinctly different ground states. At nominal ambient pressure (0.1 MPa, blue curves), the material exhibits AFM order at low temperatures, as evidenced by the Curie–Weiss-like behavior in the magnetic susceptibility χ_a (= m_a/H, with H the applied magnetic field) at elevated temperatures, followed by a sharp kink at $T_N \approx 47$ K (*Lower* panel of Fig. 2*A*) below which a distinct magnetic (easy-plane) anisotropy evolves (*SI Appendix*, Fig. S5*A*), consistent with literature results (35, 36). Measurements of relative length changes (*Upper* panel of Fig. 2*A*) reveal a small but accelerated decrease in $\Delta L_a(T, p = 0.1\,\text{MPa})/L_a$ upon cooling and a sharp kink at 47 K, reflecting a second-order phase transition at T_N. For $T < T_N$, $\Delta L_a(T, p = 0.1\,\text{MPa})/L_a$ becomes nearly temperature independent on the scale of Fig. 2*A*. In the resistivity at nominal 0.1 MPa, we find a mild increase in approaching T_N from above, followed by a kink slightly below T_N and a rapid reduction for $T < T_N$.

A significantly different behavior is revealed by applying pressure as small as $p = 81$ MPa (green curves in Fig. 2*A*). The difference from the data at 0.1 MPa begins to become visible around 70 K, below which the sample length reveals a more rapid contraction. Upon further cooling, this is followed by a drastic, though continuous, change in $\Delta L_a(T, p = 81\,\text{MPa})/L_a$, totaling an overall contraction of about one percent. As demonstrated for nonsubstituted $EuPd_2Si_2$ (*SI Appendix*, Fig. S4*A*), these are clear signatures of valence-crossover behavior. In the resistivity taken at nominal $p = 81$ MPa, the valence-crossover is reflected by a gradual increase followed by a broad maximum. The valence-crossover temperature T'_V can be identified with the inflection point on the high-temperature flank of this maximum (Fig. 2*A*, *Middle* panel), which coincides with the point of maximum slope in $\Delta L_a(T, p = 81\,\text{MPa})/L_a$ (*SI Appendix*, Fig. S6 *B* and *C*).

Downloaded from https://www.pnas.org by KARLSRUHER INSTITUT FUER TECHNOLOGIE KIT on November 18, 2026 from IP address 129.13.194.163.

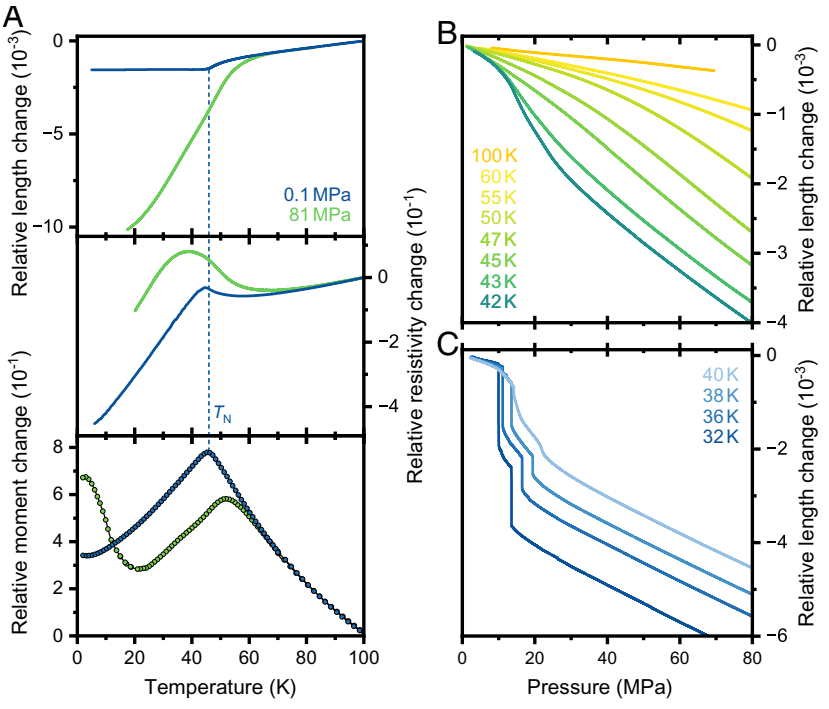


Fig. 2. Interplay between the antiferromagnetic order and valence fluctuations in $EuPd_2(Si_{0.89}Ge_{0.11})_2$. (*A*) Relative length change $\Delta L_a(T, p = \text{const.})/L_a$ along the in-plane *a* axis (*Top* panel, sample #2a), changes of the in-plane resistivity $\Delta\rho(T, p = \text{const.})/\rho$ (*Middle* panel, sample #2a_2) and changes of the magnetic moment $\Delta m_a(T, p = \text{const.})/m_a$, with the magnetic field of $H = 10$ kOe oriented along the *a* axis (*Bottom* panel, composite sample consisting of #2a_2 - #2a_4), are shown as a function of temperature at two selected constant pressures of nominal 0.1 and 81 MPa. The data were normalized to their values at 0.1 MPa and 100 K. Vertical broken line indicates the transition into AFM order at T_N under ambient-pressure ($p = 0.1$ MPa) conditions. (*B*) Relative length change $\Delta L_a(T = \text{const.}, p)/L_a$ as a function of pressure at selected temperatures above the tricritical point ($T > T_{TCP}$), showing either a continuous phase transition, associated with antiferromagnetic order for $T < T_N$, or a broad crossover behavior, associated with valence fluctuations for $T > T_N$. (*C*) Relative length change $\Delta L_a(T = \text{const.}, p)/L_a$, at selected temperatures below the tricritical point ($T < T_{TCP}$), showing discontinuous length jumps reflecting a first-order phase transition. Two distinct jumps are observed, which are attributed to sample inhomogeneities, likely resulting from slightly different Ge concentrations with two accumulation points corresponding to two (majority and minority) volume fractions (see *SI Appendix*, section B for details).

In the magnetic properties, the valence crossover manifests itself in deviations from Curie–Weiss-like behavior at elevated temperatures, followed by a rounded maximum and a low-temperature upturn (*Lower* panel of Fig. 2*A*). These features, along with the lack of anisotropy, were identified as signatures of the VF regime characterized by a maximum in $d(\chi \cdot T)/dT$ at T_V' (35) (*SI Appendix*, Fig. S6*A*).

The markedly different low-T behavior revealed for $EuPd_2(Si_{0.89}Ge_{0.11})_2$ by slightly increasing the pressure from 0.1 to 81 MPa (Fig. 2*A*), together with estimates of the electronic entropy over this pressure range performed in ref. 35, provide first indications of a phase boundary of first order separating AFM order from the VF regime, consistent with the proposed phase diagram in Fig. 1*B*. To clarify the character of this phase boundary, we performed isothermal measurements of relative length changes as a function of pressure, as illustrated in Fig. 2 *B* and *C*. Starting at an elevated temperature of 100 K, where no significant effects of charge and spin fluctuations are expected, $\Delta L_a(T = \text{const.}, p)/L_a$ decreases approximately linearly with pressure (orange curve), reflecting a normal elastic response, in accordance with Hooke's law of elasticity. However, for datasets taken at temperatures between 60 K and 47 K (light green curves), we find distinct nonlinearities, that is, a rising change in the slope, indicating an increasing softening of the lattice when entering the VF regime with increasing pressure. Upon further cooling to 42 K (dark green curves), the data reveal a kink around 14 MPa, followed by a broad s-shaped anomaly. At 40 K, first signs of jump-like anomalies are observed, which grow in size on cooling to 32 K (Fig. 2*C* and *SI Appendix*, Fig. S10). The discontinuous length changes, together with the hysteresis revealed by increasing and decreasing the pressure (*SI Appendix*, Fig. S11*A*), provide clear evidence of the first-order character of the pressure-induced transition below about 40 K; see also the discontinuous changes observed in the resistivity (*SI Appendix*, Fig. S11*B*) and the magnetic moment (*SI Appendix*, Fig. S11*C*).

The data in Fig. 2 emphasize the particularly high sensitivity of $\Delta L_a(T)/L_a$ to discriminate AFM order (small variations in $\Delta L_a(T)/L_a$) from VF (strong variations in $\Delta L_a(T)/L_a$). This observation can be used in Fig. 3*A*, which compiles $\Delta L_a(p, T)/L_a$ data obtained under isothermal (red curves) and isobaric (blue curves) conditions, to identify phase-space regions, indicated by colored surfaces, where AFM order prevails (blue surface) and those regions governed by strong VF (green surface)-an even finer differentiation is possible by considering the pressure response of $\Delta L_a/L_a$, see the discussion below. The gray area in Fig. 3*A*, spanned by the isobars at 14 and 15 MPa, corresponds to the range where the transition between AFM order and the VF regime becomes first order. A projection of the data taken at $p = \text{const.}$ conditions on the $(\Delta L_a/L_a, T)$ plane is shown in Fig. 3*B*. The figure highlights a point of bifurcation, where, below a critical temperature and depending on pressure, the system shows clear signatures of phase separation. As we argue below, this point of bifurcation, which marks the endpoint of the line of first-order phase transitions, will be used as an estimate of the location of the tricritical point (yellow-filled circle in Fig. 3 *A* and *B*), resulting in $(p_{TCP}, T_{TCP}) = (14 \pm 1\,\text{MPa}, 41 \pm 1\,\text{K})$.

The largely different strain-stress response observed along the *a* axis in reducing the temperature from 100 K to 42 K and finally 32 K, illustrated in Fig. 2 *B* and *C*, reflects drastic changes in the elastic behavior of the material within this temperature window. For a deeper inspection, we consider in Fig. 4*A* the linear isothermal *a* axis compressibility $\kappa_a = -1/L_a \cdot (dL_a/dp)_T$. At 100 K and in the pressure range investigated here, the system is in a paramagnetic state with a slightly reduced Eu moment (35). In the absence of noticeable charge and magnetic fluctuations here, $\kappa_a(p, T = 100\,\text{K})$ (yellow spheres) is small $\sim 5 \times 10^{-6}$ MPa^{-1} (consistent with results reported in ref. 32) and featureless.

Significant changes in the elastic behavior are apparent in the data taken at 60 K, and these changes become increasingly more pronounced when the temperature is reduced further to 45 K (green spheres in Fig. 4*A*), i.e., by penetrating deeper into the VF regime. The anomalous elastic behavior manifests itself in two respects. First, there is an overall growth in κ_a up to

Downloaded from https://www.pnas.org by KARLSRUHER INSTITUT FUER TECHNOLOGIE KIT on November 18, 2026 from IP address 129.13.194.163.

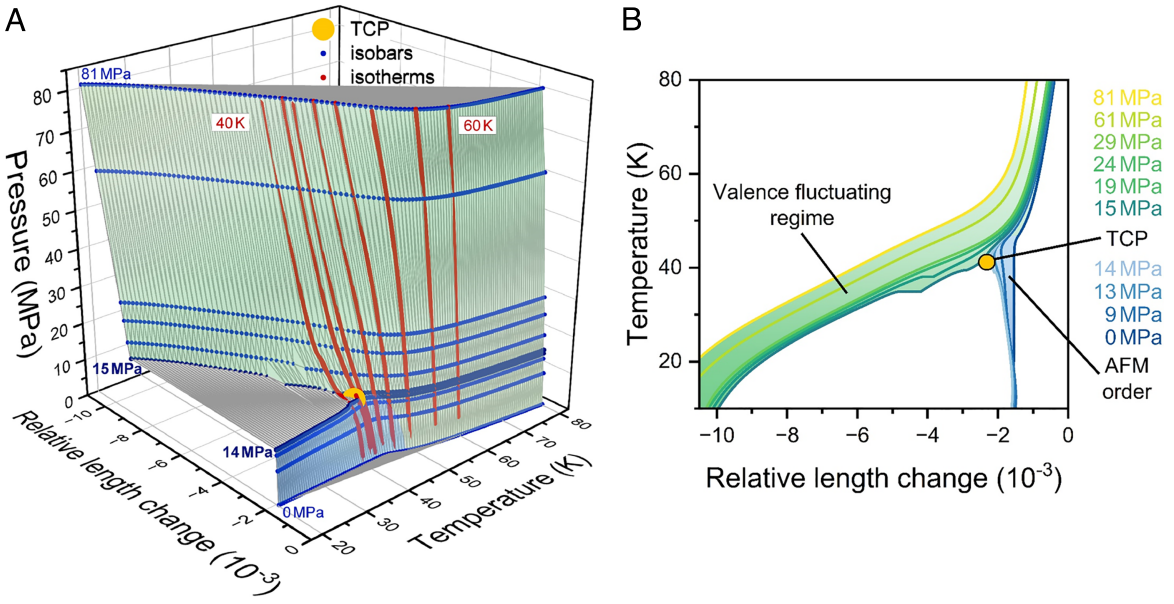


Fig. 3. Experimentally determined phase diagram of $EuPd_2(Si_{0.89}Ge_{0.11})_2$ with a tricritical point. (*A*) Three-dimensional representation of the relative length change, $\Delta L_a/L_a$, measured along the *a* axis upon variation of temperature T at p = const. (blue data points) and as a function of pressure p at T = const. (red data points) of sample #2a. The data were normalized to their values at 0.1 MPa and 100 K. The surface colored in green (blue) represents regions where valence fluctuations (antiferromagnetic order) dominate. (*B*) Projection of data taken at p = const. conditions on the $(T, \Delta L/L)$ plane. Areas colored in green (blue) correspond to regions where valence fluctuations (antiferromagnetic order) dominate. The yellow-filled circle in (*A* and *B*) marks the point where bifurcation is observed in $\Delta L_a/L_a$ and is assigned to the tricritical point $(p_{TCP}, T_{TCP}) = (14 \pm 1\,\text{MPa}, 41 \pm 1\,\text{K})$.

about one order of magnitude with decreasing temperature, a trend that also includes the behavior down to vanishingly small pressures. Second, κ_a increases with increasing pressure, with the appearance of a broad maximum that shifts to lower pressures as the temperature decreases. Based on its position in the (p, T) phase diagram (cf. Fig. 5 and *SI Appendix*, Fig. S9), the maximum in $\kappa_a(p, T = \text{const.})$ can be assigned to the valence-crossover line $T_V'(p)$.

A markedly different behavior in $\kappa_a(p, T = \text{const.})$ is revealed when the temperature is slightly reduced further, first to 43 K and then to 42 K (blue spheres), by the formation of a narrow, sharp maximum whose height increases drastically. The shape of the anomaly observed here, which reveals a rapid drop on its low-pressure flank, indicates a pressure-induced phase change. Considering the absence of discontinuities in the corresponding $\Delta L_a(p, T = \text{const.})/L_a$ vs. p data (*SI Appendix*, Fig. S10), which lack any hysteresis in increasing and decreasing pressure, we conclude that this phase change at 43 K and 42 K is of second order. The finding of a pronounced maximum in κ_a, corresponding to an extraordinarily softening of the in-plane lattice within a narrow T-p range (highlighted by the yellow area), marks the major result of this work. As we argue below, we consider this effect to reflect *elastic tricriticality*, i.e., a critical enhancement of the compressibility when tuning the system to its TCP. Note that, for a tetragonal system, the volumetric compressibility is given by $\kappa_V = 2\kappa_a + \kappa_c$, where κ_c is the corresponding *c*-axis compressibility. Consequently, a divergence of κ_a implies a divergence of κ_V. We like to point out that, in addition to the main maximum in κ_a at around 14 MPa, a second, less pronounced maximum appears at around 23 MPa in the datasets at 43 K and 42 K. We assign this feature to sample inhomogeneities, i.e., a minor volume fraction with a slightly different Ge concentration resulting in a somewhat enhanced critical pressure (*SI Appendix*, section B and Fig. S9).

It is interesting to compare the anomalous elastic properties with the corresponding response of the resistivity to pressure changes by considering the quantity $\kappa_\rho = 1/\rho \cdot (d\rho/dp)_T$. The data depicted in Fig. 4*B* have been obtained by calculating the difference quotient of $\Delta\rho(p, T = \text{const.})/\rho$ vs. p data (*SI Appendix*, Fig. S13). In fact, the κ_ρ data reveal a strikingly similar behavior to the elastic response (Fig. 4*A*) including a small and featureless $\kappa_\rho(p, T = \text{const.})$ at 100 K that grows in size as the temperature decreases to 60 K, and the appearance of a broad maximum for the data at 47 K and 45 K, which is shifted to lower pressures with decreasing temperature. Most importantly, we find the same drastic change in $\kappa_\rho(p, T = \text{const.})$ when the temperature is reduced further to 43 K, where a pronounced narrow maximum is formed, which is asymmetric in shape with a steep low-pressure flank, and the height of which increases strongly as the temperature is reduced to 42 K and 41 K. As for κ_a, the κ_ρ data also reveal a small and less pronounced feature on the high-pressure flank of the main maximum.

Discussion

Phase Diagram and Tricritical Point of $EuPd_2(Si_{0.89}Ge_{0.11})_2$. Fig. 5 summarizes in a (p, T) phase diagram the positions of the various phase transitions and crossover anomalies of $EuPd_2(Si_{0.89}Ge_{0.11})_2$ revealed by measurements of expansivity (cf. Fig. 3 and *SI Appendix*, Figs. S7 and S10), magnetic moment (cf. Fig. 2*A* and *SI Appendix*, Figs. S6 and S8), and resistivity (cf. Figs. 2*A* and 4*B* and *SI Appendix*, Figs. S12 and S13). The figure also displays the variation of the *a*-axis compressibility, κ_a, in a colored contour plot. On the low-pressure side, the diagram shows a range of AFM order below the Néel temperature $T_N \approx 47$ K (blue symbols connected by the white line), which remains practically constant for $p \lesssim 12$ MPa [see *SI Appendix*, Figs. S5 and S7 for the determination of $T_N(p)$], consistent with results in ref. 35. Apart from the region surrounding T_N, the magnetically ordered phase is characterized by a relatively small κ_a (deep blue area), of size

Downloaded from https://www.pnas.org by KARLSRUHER INSTITUT FUER TECHNOLOGIE KIT on November 18, 2026 from IP address 129.13.194.163.

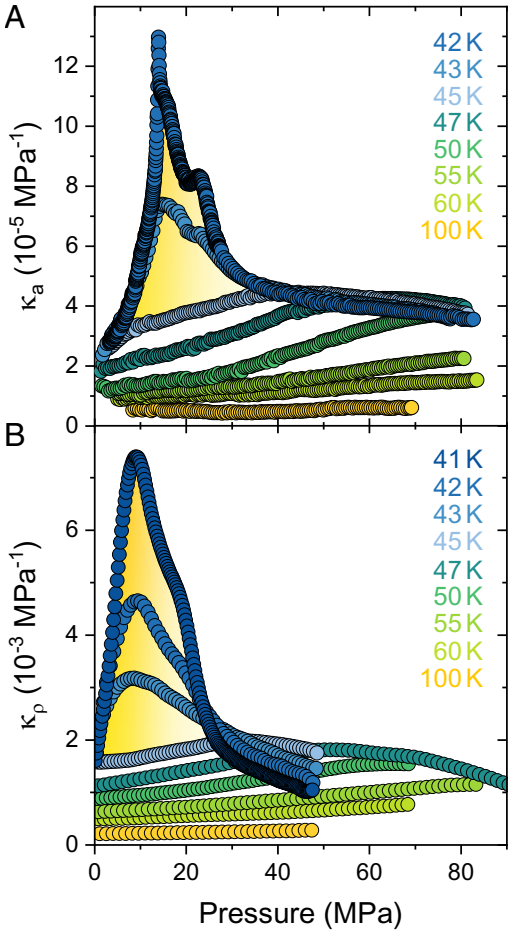


Fig. 4. Effect of pressure on approaching the tricritical point. Compilation of experimental data on $EuPd_2(Si_{0.89}Ge_{0.11})_2$ derived from pressure sweeps at selected fixed temperatures. (*A*) Linear isothermal *a*-axis compressibility, $\kappa_a = -1/L_a \cdot (dL_a/dp)_T$, of sample #2a. (*B*) Pressure derivative of the in-plane electrical resistivity, $\kappa_\rho = 1/\rho \cdot (d\rho/dp)_T$, of sample #2a_2, a fragment of #2a, for the same selected temperatures as in (A) using the same color code. The differentials in (*A* and *B*) were approximated by calculating the difference quotients. Areas highlighted in yellow indicate the strong increase in the pressure response revealed upon approaching the tricritical point. The two-peak feature can be attributed to inhomogeneities in the sample, which are presumably due to a slightly different Ge ratio with two accumulation points corresponding to two (majority and minority) volume fractions (see *SI Appendix*, section B for details).

$\kappa_a \lesssim 1 \cdot 10^{-5}\,\mathrm{MPa}^{-1}$. This value is about twice as large as that revealed for $EuPd_2(Si_{0.89}Ge_{0.11})_2$ at elevated temperatures (100 K) and found in other Eu-containing 122 systems with nonfluctuating (stable) Eu valence (40). With further increasing pressure, T_N begins to decrease while simultaneously losing its clear signature in a temperature-dependent experiment (*SI Appendix*, Fig. S7*A*). The reason for this is likely two-fold. First, it may indicate a rapid drop in $T_N(p)$ in an almost vertical manner, making temperature-dependent studies insensitive. Second, on decreasing the temperature in this part of the phase diagram, there is a large and even further growing contribution from VF surrounding the valence crossover (area with a green-to-yellow color change), which may obscure any signature of AFM order, even in pressure-dependent experiments. However, upon further cooling to below 45 K - that is, entering the region where κ_a becomes strongly enhanced (red area) - the data at 43 K and 42 K in fact do reveal sharp peaks as a function of pressure (blue-green hexagons), reflecting a second-order phase transition. We assign these features to a pressure-induced phase transition associated with $T_N(p)$; see the occurrence of magnetic anisotropy in *SI Appendix*, Fig. S8*A*, in support of this assignment.

On the high-pressure side of the phase diagram in Fig. 5, VF prevail manifesting themselves in broadened maxima in the temperature and pressure dependence of various quantities (green symbols), which can be assigned to the crossover temperature $T'_V(p)$ (green dashed line, and see Fig. 4 and *SI Appendix*, Figs. S6, S7, and S12). As a function of p, this crossover temperature increases with a slope $dT'_V/dp = (90-100)$ K/GPa, consistent with previous observations in ref. 35. The regime governed by VF (green area) is characterized by a significantly, i.e., by an order of magnitude enhanced $\kappa_a \approx 5 \cdot 10^{-5}\,\mathrm{MPa}^{-1}$, making this quantity a highly sensitive thermodynamic probe for the detection of even weak signatures of VF throughout the phase diagram. For temperatures $T \lesssim 40$ K, the phase diagram shows a line of first-order phase transitions (black, semitransparent line), as evidenced by discontinuities and hysteretic behavior (black, shaded regime surrounding the black line) in various, pressure-dependent probes, notably $\Delta L_a/L_a$, studied under isothermal conditions (Figs. 2 and 3 and *SI Appendix*, Figs. S10 and S11). The phase diagram highlights a tricritical point at $(p_{TCP}, T_{TCP}) = (14 \pm 1\,\mathrm{MPa}, 41 \pm 1\,\mathrm{K})$ as a consequence of the second-order transition line $T_N(p)$ turning first order upon merging with the crossover line $T'_V(p)$, consistent with the proposed phase diagram in Fig. 1*B*.

While key aspects of the phase diagram shown in Fig. 5 and its implications for a variety of strongly correlated electron systems based on Ce (41–43) and Eu (44–47) have been previously discussed (20, 21), we would like to emphasize that clear experimental evidence of a first-order phase transition including a TCP has been missing thus far. Therefore, the present study on $EuPd_2(Si_{0.89}Ge_{0.11})_2$ provides a prime example of the proposed VF-induced collapse of AFM order, leading to a TCP, which enables exploration of the interplay of strong fluctuations in charge, lattice, and spin degrees of freedom.

Universality of Elastic Tricriticality. The sensitivity of the phase diagram in Fig. 5 with respect to hydrostatic pressure already implies a strong coupling of magnetic and valence fluctuations to the crystal lattice of $EuPd_2(Si_{0.89}Ge_{0.11})_2$. In the following, we argue theoretically that this elastic coupling qualitatively modifies the tricritical behavior and changes its universality class, resulting in elastic tricriticality. The key signature of elastic tricriticality is a vanishing elastic bulk modulus or, equivalently, a diverging compressibility.

The focus of our interest is the component ε of the strain tensor that transforms as a volumetric singlet of the irreducible representations of the crystal group. This singlet will generically couple to the energy density ϕ^2 of the order parameter ϕ associated with the symmetry breaking at a phase transition,

$$\mathcal{L}_{\phi-\varepsilon} = \lambda\,\phi^2\varepsilon, \qquad [1]$$

where λ is the elastic coupling. Whether this coupling influences the critical behavior of a continuous phase transition in a fundamental manner follows from arguments given by Rice (48). In second-order perturbation theory in λ, the coupling leads to a correction to the bulk modulus $\delta K \sim -\lambda^2\langle\phi^2\phi^2\rangle$ that is proportional to the energy density autocorrelation function of the order parameter and thus proportional to the critical part of the specific heat c_{cr}. As the phase transition is approached, e.g., as a function of temperature $c_{cr} \sim |T - T_c|^{-\alpha}$ varies

Downloaded from https://www.pnas.org by KARLSRUHER INSTITUT FUER TECHNOLOGIE KIT on November 18, 2026 from IP address 129.13.194.163.

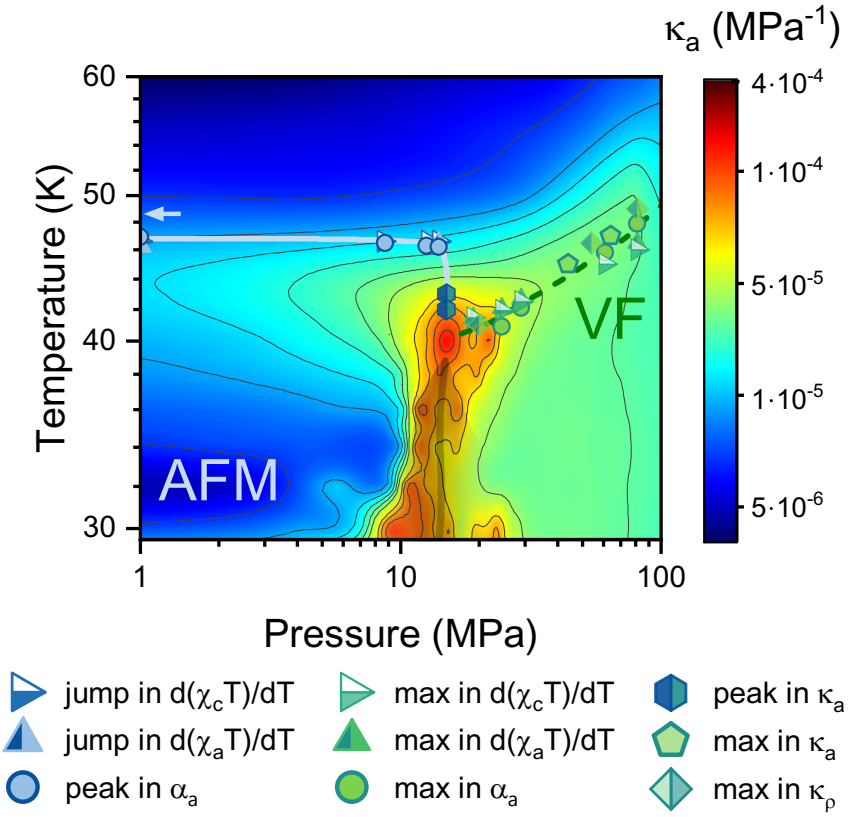


Fig. 5. Phase diagram and in-plane compressibility of $EuPd_2(Si_{0.89}Ge_{0.11})_2$ in the vicinity of its tricritical point. Blue data points correspond to second-order phase transition anomalies at the formation of antiferromagnetic order at $T_N(p)$ (white line), including i) a jump-like anomaly in $d(\chi \cdot T)/dT$, where χ is the magnetic susceptibility measured in a magnetic field of $H = 10$ kOe, aligned along (χ_a) and perpendicular (χ_c) to the in-plane a axis, yielding an easy-plane anisotropy (see *SI Appendix*, Fig. S5*A* and ref. 35), and ii) a pronounced peak in the coefficient of thermal expansion, $\alpha_a = L_a^{-1}(dL_a/dT)$ (*SI Appendix*, Fig. S5*B*). Green symbols correspond to the positions of broad maxima associated with valence-crossover behavior at $T_V'(p)$ (green dashed line) revealed in $d(\chi \cdot T)/dT$, in α_a, in the in-plane compressibility κ_a and in the pressure derivative of the in-plane resistivity κ_ρ. The black semitransparent line marks the first-order phase transition separating AFM order at low pressure from a regime of strong VF at higher pressures. The black shaded area indicates the regime where hysteresis effects were observed in p sweeps; see *SI Appendix*, Fig. S9 for a corresponding diagram which includes also data for the minor volume fraction with slightly enhanced critical pressure. The color plot shows the anomalous contribution to the in-plane compressibility κ_a obtained after subtracting the (noncritical) background contribution determined at $T = 100$ K.

with the specific heat exponent α. For a positive $\alpha > 0$, this negative correction to the bulk modulus diverges, i.e., the total bulk modulus vanishes before the critical temperature is reached. The elastic coupling λ thus becomes nonperturbative and it can be shown that the crystal indeed becomes elastically unstable (48). A nonperturbative elastic coupling necessarily occurs only for certain universality classes of second-order critical points, e.g., the Ising universality class in spatial dimensions $d = 3$ where elastic criticality will eventually prevail. In contrast, for the Heisenberg universality class in $d = 3$ the specific heat exponent is negative, and the elastic coupling remains perturbative for small λ.

However, at the TCP in $d = 3$ the specific heat exponent of the theory at zeroth order in λ is given by the Gaussian value $\alpha = 1/2$ (49). The elastic coupling at tricriticality is thus always nonperturbative. As a consequence, the elastic coupling eventually induces a crossover to a regime where the tricriticality is strongly coupled to elasticity. Technically speaking, in the framework of the renormalization group the elastic coupling destabilizes the Gaussian tricritical fixed point and gives rise to an elastic tricritical fixed point that governs the tricritical behavior and reflects the change of the universality class (50), see *SI Appendix*, section I and Fig. S14 for details. At elastic tricriticality, the compressibility diverges with a characteristic critical exponent.

At the TCP of $EuPd_2(Si_{0.89}Ge_{0.11})_2$ the compressibility is indeed strongly enhanced by about a factor of 20 as compared to its value at higher temperatures, see Fig. 5. This is strong evidence that elastic tricriticality prevails in $EuPd_2(Si_{0.89}Ge_{0.11})_2$ sufficiently close to its TCP. Although the observations in Fig. 4*A* are consistent with a divergent compressibility at the TCP, our data do not yet allow for a reliable extraction of the associated critical exponent.

Charge Transport Close to Elastic Tricriticality. We now turn to the resistivity and discuss its pressure dependence. Close to the TCP, its variation with pressure, $\kappa_\rho = 1/\rho \cdot (d\rho/dp)_T$ is strikingly similar to the behavior of the compressibility κ_a, see Fig. 4*B*. The close resemblance between κ_ρ and κ_a close to the TCP suggests that tricritical fluctuations dominate not only the thermodynamic response but also charge transport.

This can be rationalized following arguments put forward by Fisher and Langer (51). Here, one assumes that the transport relaxation rate is dominated by short-range critical fluctuations such that the critical part of the resistivity ρ_{cr} obtains a singular temperature dependence proportional to the energy density of the order parameter $\rho_{cr} \sim \langle \phi^2 \rangle$, which in turn, via the elastic coupling, is also proportional to the critical part of the volume change $\Delta V_{cr} \sim \langle \phi^2 \rangle$. Consequently, close to the TCP, when critical contributions dominate, the pressure derivative of the resistivity will behave similarly to the compressibility, $\frac{1}{\rho}\partial_p \rho \sim \kappa$, which accounts for the experimental observations. As κ_ρ and κ_a are similarly enhanced close to the valence crossover $T_V'(p)$, it appears that this argument also applies to some extent to the valence fluctuations.

Summary and Outlook

In summary, by the application of various experimental probes to $EuPd_2(Si_{0.89}Ge_{0.11})_2$, especially through measurements of relative length changes under control of temperature and He-gas pressure, a tricritical point has been identified that results from the interplay of long-range antiferromagnetic order and strong valence fluctuations. The tunability of the material's ground state with pressure is associated with strong tricritical anomalies in elastic properties, notably a compressibility that at the TCP is strongly enhanced by about a factor of 20 as

Downloaded from https://www.pnas.org by KARLSRUHER INSTITUT FUER TECHNOLOGIE KIT on November 18, 2026 from IP address 129.13.194.163.

compared to its value at higher temperature. We argued that this implies a strong coupling between tricritical fluctuations and elastic degrees of freedom resulting in elastic tricriticality, where the tricritical point of the magnetic phase transition coincides with an isostructural elastic instability of the crystal lattice, i.e., a diverging compressibility. In addition, we found that the pressure derivative of the resistivity exhibits a close resemblance to the compressibility, which we interpreted as evidence for short-range critical fluctuations that dominate charge transport close to the TCP (51).

Theoretically speaking, elastic tricriticality is specified by a critical fixed point in the renormalization group sense with a diverging correlation length and characteristic critical exponents, see *SI Appendix*, section I. This is in contrast to the elastic criticality found at critical endpoints of valence and Mott transitions, which are only mean-field like without a diverging correlation length. This difference is rooted in the distinct coupling to the volumetric strain singlet ε. Whereas for the CEP a bilinear coupling $\varepsilon\,\psi$ between the strain singlet and the Ising order parameter ψ of the CEP is allowed (18), such a bilinear coupling is symmetry forbidden for the TCP. The bilinear coupling preempts criticality, cuts off the correlation length and renders the CEP mean-field like. In contrast, such a preemption is not possible for the TCP because it is still connected to a line of second-order phase transitions even in the presence of the elastic coupling Eq. **1**. As a result, electronic and elastic degrees of freedom are nonperturbatively intertwined at elastic tricriticality resulting in nontrivial critical scaling behavior.

The arguments for the emergence of elastic tricriticality are very general. Although $EuPd_2(Si_{0.89}Ge_{0.11})_2$ provides a prime example associated with antiferromagnetic ordering, we expect that elastic tricriticality will also be relevant to numerous other materials. This includes pressure-induced tricritical points in itinerant ferromagnets (52, 53), such as UGe_2 (54), and $LaCrGe_3$ (55), as well as in several ferroelectrics as, e.g., in KH_2PO_4 (56), SbSI (57), and NH_4Cl (58). In fact, the results of the relative length change in NH_4Cl are consistent with a divergent compressibility when approaching the material's TCP (58). It should also extend to tricritical points induced by magnetic field but that are amenable to pressure tuning like in $NbFe_2$ (59) and $FeCl_2$. In the latter a substantial softening of a longitudinal elastic mode near the TCP was already observed (60).

In general, whenever a line of first-order phase transitions can be crossed by the application of pressure, and this line terminates at a critical point, the associated criticality will be strongly influenced by elasticity. This applies to critical endpoints, e.g., for the Mott transition (18), to tricritical points considered here, but also to other higher-order critical points, for example, bicritical points found, e.g., close to spin–flop transitions. Under certain conditions, elasticity will also be nonperturbatively involved in quantum versions of such pressure-tuned higher-order critical points (61–63), for example, quantum bicritical points (64) or quantum tricritical points (59).

Materials and Methods

Crystal Growth and Selection of Samples. Ge-substituted $EuPd_2Si_2$ was grown using the Czochralski method as previously described in refs. 36 and 65. The investigated $EuPd_2(Si_{1-x}Ge_x)_2$ crystal MP807 was obtained from an initial melt with a nominal Ge concentration of $x_{nom} = 0.2$. As shown in ref. 36, the Ge incorporation rate in the grown sample is about 50% for this substitution level which leads to an enrichment of Ge in the melt in the course of the growth. All measurements described in the main text were carried out on samples cut from the same large mother crystal MP807, see *SI Appendix*, Table S1 and Fig. S2 for details, including crystal structure, an overview of all samples investigated, and sample characterization.

Energy Dispersive X-Ray Spectroscopy. Energy dispersive X-ray (EDX) analysis was used to analyze the sample composition and germanium incorporation using a Zeiss DSM940A scanning electron microscope with an EDAX detector. The statistical relative error of the Ge concentration in the EDX measurement is typically 7–10 % (see Tab. I in ref. 36), which limits the determination of small Ge concentrations in the sample. The substitution level x_{EDX} was obtained by averaging multiple measurements taken at different positions at a certain distance from the seed of a single crystal.

Capacitive Dilatometry. Measurements of the relative length change $\Delta L_a/L_a = [L_a(T) - L_a(T_0)]/L_a(T_0)$, L_a being the sample length along the in-plane a axis and T_0 a reference temperature, with a resolution $\Delta L/L \leq 10^{-10}$, were carried out using a capacitive dilatometer [Kuechler Innovative Measurement Technology (66)] installed in a CuBe pressure cell (Unipress Equipment Division, Institute of High Pressure Physics, Polish Academy of Science). The pressure cell is connected via a CuBe capillary to a compressor unit with a 30 MPa helium gas bottle serving as a gas reservoir. The system enables measurements of relative length changes to be performed in various modes, including temperature sweeps at constant pressure, as well as pressure sweeps at constant temperature; see refs. 37 and 38 for details on measurements of relative length changes under variable He-gas pressure. Thermal expansion measurements were performed at a heating/cooling rate of $\pm$ 3 K/h, ensuring a pressure stability of $\Delta p/p \lesssim 0.5\%$ at $p \leq 30$ MPa and $\Delta p/p \lesssim 5\%$ at $p > 30$ MPa. The pressure values given throughout the manuscript are nominal values that reflect the pressure set at approximately 100 K. The actual pressures at the base temperature are slightly lower due to the isochoric cooling of the cell. Pressure sweeps were performed at a rate of $\sim \pm 3$ MPa/h, with a temperature stability of $\Delta T/T \lesssim 0.1\%$. The use of a capacitive dilatometer under variable (He-gas) pressure requires the knowledge of the dielectric function of the pressure-transmitting medium $\varepsilon_r^{He}(T,p)$. To this end, $\varepsilon_r^{He}(T,p)$ was determined by measuring the change in the capacitance of the dilatometer for a reference material (high-purity (5N), oxygen-free copper of 4.5 mm length) along the same T-p-trajectory at which the $\Delta L(T,p)/L$ data were collected for the samples under investigation, see ref. 38 for details. The capacitive dilatometry implies a small force ΔF acting on the sample along the measuring direction given by $\Delta F/\Delta C \approx 1.1$ N/pF, which depends on the adjusted starting capacitance $C_0 = C_{empty} + \Delta C$, with C_{empty} the capacitance of the empty cell without a sample. For the present experiment $\Delta C \approx 9$ pF, which for the geometry of the sample used resulted in a uniaxial pressure of $p_a \approx 8$ MPa.

DC-Susceptibility. The magnetic susceptibility $\chi = m/H$, with H the magnetic field, is derived from measurements of the magnetic moment $\Delta m = m(T) - m(T_0)$, with T_0 a reference temperature, using a commercial superconducting quantum interference device (SQUID) magnetometer (Quantum Design, MPMS XL), equipped with a CuBe pressure cell (Unipress Equipment Division, Institute of High Pressure Physics, Polish Academy of Science). The pressure cell is connected by a CuBe capillary to a compressor and a helium gas bottle (67). The pressure is recorded by a digital manometer (Keller AG, Leo 5) with a resolution of $|p| \leq 0.1$ MPa, similar to the setup used for dilatometric investigations. Typically, a rate of $\pm$1 K/min was used for the temperature sweeps, and a rate of $\pm$0.5 MPa/min was used for the pressure sweeps.

AC-Resistivity. The resistivity $\Delta\rho = \rho(T) - \rho(T_0)$, with T_0 a reference temperature, was measured in a four-terminal configuration by using an AC-resistance bridge LR700 from Linear Research operating at a frequency of 15.9 Hz. Gold wires (25μm diameter) were attached along the a axis of the sample using silver paste. For measurements under hydrostatic He-gas pressure,

Downloaded from https://www.pnas.org by KARLSRUHER INSTITUT FUER TECHNOLOGIE KIT on November 18, 2026 from IP address 129.13.194.163.

a CuBe pressure cell connected to a compressor unit (Unipress Equipment Division, Institute of High Pressure Physics, Polish Academy of Science) was used via a CuBe capillary. The pressure is recorded by a digital manometer (WIKA, CPG 1500) with a resolution of $|p| \leq 0.1$ MPa. Temperature sweeps were performed at ± 0.2 K/min, and pressure sweeps at ± 0.5 MPa/min.

Data, Materials, and Software Availability. Processed data underlying the figures data have been deposited in Goethe University data repository (GUDe) (68). All other data are included in the manuscript and/or *SI Appendix*.

ACKNOWLEDGMENTS. We would like to thank Ch. Geibel, J. Schmalian, and N. Sander for valuable discussions, as well as S. Hartmann for her support in the early stage of the experiments. This work was supported by the Deutsche Forschungsgemeinschaft (German Research Foundation) through TRR 288–422213477 (projects A01, A03, A06, and A11).

1. N. F. Mott, *Metal-Insulator Transitions* (Taylor & Francis, ed. 2, 1990).
2. D. B. McWhan, T. M. Rice, J. P. Remeika, Mott transition in Cr-doped V_2O_3. *Phys. Rev. Lett.* **23**, 1384–1387 (1969).
3. A. Jayaraman, D. B. McWhan, J. P. Remeika, P. D. Dernier, Critical behavior of the mott transition in Cr-doped V_2O_3. *Phys. Rev. B* **2**, 3751–3756 (1970).
4. K. Kanoda, Recent progress in NMR studies on organic conductors. *Hyperfine Interact.* **104**, 235–249 (1997).
5. A. Jayaraman, Fusion curve of cerium to 70 kilobar and phenomena associated with supercritical behavior of FCC cerium. *Phys. Rev.* **137**, A179–A182 (1965).
6. J. M. Lawrence, M. C. Croft, R. D. Parks, Critical behavior at a valence instability. *Phys. Rev. Lett.* **35**, 289–292 (1975).
7. D. C. Koskenmaki, K. A. Gschneidner, "Chapter 4 cerium" in *Metals, Handbook on the Physics and Chemistry of Rare Earths*, K. A. Gschneidner, Jr., L. Eyring, Eds. (Elsevier, 1978), vol. 1, pp. 337–377.
8. J. M. Robinson, Valence transitions and intermediate valence states in rare earth and actinide materials. *Phys. Rep.* **51**, 1–62 (1979).
9. R. D. Parks, Mixed valence phenomena: An overview. *Hyperfine Interact.* **25**, 565–581 (1985).
10. C. Castellani, C. D. Castro, D. Feinberg, J. Ranninger, New model hamiltonian for the metal-insulator transition. *Phys. Rev. Lett.* **43**, 1957–1960 (1979).
11. G. Kotliar, E. Lange, M. J. Rozenberg, Landau theory of the finite temperature Mott transition. *Phys. Rev. Lett.* **84**, 5180 (2000).
12. R. A. Cowley, Acoustic phonon instabilities and structural phase transitions. *Phys. Rev. B* **13**, 4877–4885 (1976).
13. M. Dzero, M. R. Norman, I. Paul, C. Pépin, J. Schmalian, Erratum: Quantum critical end point for the kondo volume collapse model [Phys. Rev. Lett. **97**, 185701 (2006)]. *Phys. Rev. Lett.* **104**, 119901 (2010).
14. A. Hackl, M. Vojta, Kondo volume collapse, Kondo breakdown, and Fermi surface transitions in heavy-fermion metals. *Phys. Rev. B* **77**, 134439 (2008).
15. E. Gati *et al.*, Breakdown of Hooke's law of elasticity at the Mott critical endpoint in an organic conductor. *Sci. Adv.* **2**, e1601646 (2016).
16. P. Majumdar, H. R. Krishnamurthy, Lattice contraction driven insulator-metal transition in the $d = \infty$ local approximation. *Phys. Rev. Lett.* **73**, 1525–1528 (1994).
17. S. R. Hassan, A. Georges, H. R. Krishnamurthy, Sound velocity anomaly at the mott transition: Application to organic conductors and V_2O_3. *Phys. Rev. Lett.* **94**, 036402 (2005).
18. M. Zacharias, L. Bartosch, M. Garst, Mott metal-insulator transition on compressible lattices. *Phys. Rev. Lett.* **109**, 176401 (2012).
19. T. Thyzel *et al.*, Absence of critical fluctuations at the bandwidth-controlled Mott transition in a molecular conductor. *Phys. Rev. B* **112**, L121101 (2025).
20. S. Watanabe, K. Miyake, Origin of drastic change of fermi surface and transport anomalies in $CeRhIn_5$ under pressure. *J. Phys. Soc. Jpn.* **79**, 033707 (2010).
21. S. Watanabe, K. Miyake, Roles of critical valence fluctuations in Ce- and Yb-based heavy fermion metals. *J. Phys. Condens. Matter* **23**, 094217 (2011).
22. H. Q. Yuan *et al.*, Observation of two distinct superconducting phases in $CeCu_2Si_2$. *Science* **302**, 2104–2107 (2003).
23. C. U. Segre *et al.*, Valence instability in $Eu(Pd_{1-x}Au_x)_2Si_2$: The global phase diagram. *Phys. Rev. Lett.* **49**, 1947–1950 (1982).
24. E. R. Bauminger *et al.*, Charge fluctuations in europium in metallic $EuCu_2Si_2$. *Phys. Rev. Lett.* **30**, 1053–1056 (1973).
25. Y. Ōnuki, M. Hedo, F. Honda, Unique electronic states of Eu-based compounds. *J. Phys. Soc. Jpn.* **89**, 102001 (2020).
26. Y. Lai, J. Y. Chan, R. E. Baumbach, Electronic landscape of the *f*-electron intermetallics with the $ThCr_2Si_2$ structure. *Sci. Adv.* **8**, eabp8264 (2022).
27. H. Wada *et al.*, Thermal expansion and electrical resistivity of $EuNi_2(Si_{1-x}Ge_x)_2$. *J. Phys. Soc. Jpn.* **68**, 950–953 (1999).
28. H. Wada, M. F. Hundley, R. Movshovich, J. D. Thompson, Pressure effect on the valence transition of $EuNi_2(Ge_{1-x}Si_x)_2$. *Phys. Rev. B* **59**, 1141–1144 (1999).
29. A. Mitsuda, S. Hamano, N. Araoka, H. Yayama, H. Wada, Pressure-induced valence transition in antiferromagnet $EuRh_2Si_2$. *J. Phys. Soc. Jpn.* **81**, 023709 (2012).
30. Y. Ōnuki *et al.*, Divalent, trivalent, and heavy fermion states in Eu compounds. *Philos. Mag.* **97**, 3399–3414 (2016).
31. E. V. Sampathkumaran *et al.*, A new and unique Eu-based mixed valence system: $EuPd_2Si_2$. *J. Phys. C Solid State Phys.* **14**, L237–L241 (1981).
32. B. Batlogg *et al.*, *Valence Instabilities* (North-Hollond, Amsterdam, 1982), p. 229.
33. E. Kemly *et al.*, Mössbauer effects and L_{III} absorption measurements on $EuPd_2Si_2$. *J. Magn. Magn. Mater.* **47–48**, 403–406 (1985).
34. O. Fedchenko *et al.*, Valence transition induced changes of the electronic structure in $EuPd_2Si_2$. *Phys. Rev. B* **109**, e06421 (2024).
35. B. Wolf *et al.*, Pressure study on the interplay between magnetic order and valence crossover in $EuPd_2(Si_{1-x}Ge_x)_2$. *Phys. Rev. B* **107**, 245147 (2023).
36. M. Peters *et al.*, From valence fluctuations to long-range magnetic order in $EuPd_2(Si_{1-x}Ge_x)_2$ single crystals. *Phys. Rev. Mater.* **7**, 1–12 (2023).
37. R. S. Manna, B. Wolf, M. de Souza, M. Lang, High-resolution thermal expansion measurements under helium-gas pressure. *Rev. Sci. Instrum.* **83**, 085111 (2012).
38. Y. Agarmani *et al.*, Advanced technique for measuring relative length changes under control of temperature and helium-gas pressure. *Rev. Sci. Instrum.* **93**, 113902 (2022).
39. H. Jhans, M. Croft, E. Kemly, B. Grier, C. U. Segre, *X-Ray Diffraction and Mössbauer Effect Measurements near a Valence Transition* (Springer, US, 1987), pp. 655–658.
40. H. J. Hesse, R. Lübbers, M. Winzenick, H. Neuling, G. Wortmann, Pressure and temperature dependence of the Eu valence in $EuNi_2Ge_2$ and related systems studied by mössbauer effect, x-ray absorption and x-ray diffraction. *J. Alloys Compd.* **246**, 220–231 (1997).
41. T. Park *et al.*, Hidden magnetism and quantum criticality in the heavy fermion superconductor $CeRhIn_5$. *Nature* **440**, 65–68 (2006).
42. T. Park *et al.*, Isotropic quantum scattering and unconventional superconductivity. *Nature* **456**, 366–368 (2008).
43. G. W. Scheerer, G. Giriat, Z. Ren, G. Lapertot, D. Jaccard, High-pressure study of the ground- and superconducting-state properties of $CeAu_2Si_2$. *J. Phys. Soc. Jpn.* **86**, 064710 (2017).
44. S. Fukuda *et al.*, Application of doniach diagram on valence transition in $EuCu_2(Si_xGe_{1-x})_2$. *J. Phys. Soc. Jpn.* **72**, 3189–3196 (2003).
45. Z. Hossain *et al.*, Antiferromagnetism, valence fluctuation, and heavy-fermion behavior in $EuCu_2(Ge_{1-x}Si_x)_2$. *Phys. Rev. B* **69**, 014422-1–014422-9 (2004).
46. J. Gouchi *et al.*, Quantum criticality of valence transition for the unique electronic state of antiferromagnetic compound $EuCu_2Ge_2$. *J. Phys. Soc. Jpn.* **89**, 053703 (2020).
47. M. A. Ahmida *et al.*, Interplay between valence fluctuations and lattice instabilities across the quantum phase transition in $EuCu_2(Ge_{1-x}Si_x)_2$. *Phys. Rev. B* **102**, 155110-1–155110-13 (2020).
48. O. K. Rice, Thermodynamics of phase transitions in compressible solid lattices. *J. Chem. Phys.* **22**, 1535–1544 (1954).
49. E. K. Riedel, F. J. Wegner, Tricritical exponents and scaling fields. *Phys. Rev. Lett.* **29**, 349–352 (1972).
50. F. J. Wegner, Magnetic phase transitions on elastic isotropic lattices. *J. Phys. C Solid State Phys.* **7**, 2109–2125 (1974).
51. M. E. Fisher, J. S. Langer, Resistive anomalies at magnetic critical points. *Phys. Rev. Lett.* **20**, 665–668 (1968).
52. M. Brando, D. Belitz, F. M. Grosche, T. R. Kirkpatrick, Metallic quantum ferromagnets. *Rev. Mod. Phys.* **88**, 025006 (2016).
53. J. Flouquet *et al.*, Trends in heavy fermion matter. *J. Phys. Conf. Ser.* **273**, 012001 (2011).
54. V. Taufour, D. Aoki, G. Knebel, J. Flouquet, Tricritical point and wing structure in the itinerant ferromagnet UGe_2. *Phys. Rev. Lett.* **105**, 217201 (2010).
55. U. S. Kaluarachchi, S. L. Bud'ko, P. C. Canfield, V. Taufour, Tricritical wings and modulated magnetic phases in $LaCrGe_3$ under pressure. *Nat. Commun.* **8**, 546 (2017).
56. V. H. Schmidt, A. B. Western, A. G. Baker, Tricritical point in kh_2po_4. *Phys. Rev. Lett.* **37**, 839–842 (1976).
57. P. S. Peercy, Raman scattering near the tricritical point in SbSI. *Phys. Rev. Lett.* **35**, 1581–1584 (1975).
58. B. B. Weiner, C. W. Garland, Order-disorder phenomena. VII. Critical variations in the length of nh_4cl single crystals at high pressures. *J. Chem. Phys.* **56**, 155–165 (1972).
59. S. Friedemann *et al.*, Quantum tricritical points in $NbFe_2$. *Nat. Phys.* **14**, 62–67 (2017).
60. G. Gorodetsky, A. Shaulov, V. Volterra, J. Makovsky, Sound propagation near the tricritical point of $FeCl_2$. *Solid State Commun.* **25**, 1129–1131 (1978).
61. P. Chandra, P. Coleman, M. A. Continentino, G. G. Lonzarich, Quantum annealed criticality: A scaling description. *Phys. Rev. Res.* **2**, 043440 (2020).
62. A. Samanta, E. Shimshoni, D. Podolsky, Phonon-induced modification of quantum criticality. *Phys. Rev. B* **106**, 035154 (2022).
63. S. Sarkar, L. Franke, N. Grivas, M. Garst, Quantum criticality on a compressible lattice. *Phys. Rev. B* **108**, 235126 (2023).
64. Y. Tokiwa, M. Garst, P. Gegenwart, S. L. Bud'ko, P. C. Canfield, Quantum bicriticality in the heavy-fermion metamagnet ybagge. *Phys. Rev. Lett.* **111**, 116401 (2013).
65. K. Kliemt *et al.*, Influence of the Pd-Si ratio on the valence transition in $EuPd_2Si_2$ single crystals. *Cryst. Growth Des.* **22**, 5399–5406 (2022).
66. R. Küchler, T. Bauer, M. Brando, F. Steglich, A compact and miniaturized high resolution capacitance dilatometer for measuring thermal expansion and magnetostriction. *Rev. Sci. Instrum.* **83**, 095102 (2012).
67. B. Wolf *et al.*, Combined experimental and theoretical study of hydrostatic He-gas pressure effects in α-$RuCl_3$. *Phys. Rev. B* **106**, 13178 (2022).
68. Y. Agarmani *et al.*, Elastic tricriticality at the collapse of magnetic order in a valence fluctuating Eu-based compound, GUDe. https://doi.org/10.25716/gude.0nrr-1vk8. Deposited 29 October 2026.

Downloaded from https://www.pnas.org by KARLSRUHER INSTITUT FUER TECHNOLOGIE KIT on November 18, 2026 from IP address 129.13.194.163.